Ceramics International 44 (2018) 703–711

Contents lists available at ScienceDirect

Ceramics International

journal homepage: www.elsevier.com/locate/ceramint

Experimental and theoretical study on the structural, electrical and optical properties of tantalum-doped ZnO nanoparticles prepared via sol-gel acetate route

Diego Richard*, Mariano Romero, Ricardo Faccio

Centro NanoMat/DETEMA, Facultad de Química, Universidad de la República (UdelaR), CC 1157, Montevideo, Uruguay

ARTICLE INFO

Keywords:
ZnO
Sol-gel processes
Impurities in semiconductors
Tantalum
ab initio calculations

ABSTRACT

Pure and Ta-doped ZnO were prepared by the sol-gel method in acetic medium using different annealing temperature treatments. The effects of low Ta doping on the crystallinity and electrical properties of ZnO nanoparticles were analyzed by means of X-ray diffraction and micro-Raman, UV–visible, and impedance spectroscopies.

We also performed first principles calculations in order to study the predicted changes in the structural, vibrational and electronic properties induced by the inclusion of the impurities, and to complement the experimental measurements.

We showed that above thermal treatments at 600 °C the precursor samples take the hexagonal wurtzite ZnO phase with high crystallinity. For the doped samples, we found that the synthesizing method has good Ta doping efficiency of the ZnO host structure. Also, Ta doping substantially decreases the resistivity compared to pure ZnO. These results confirm that Ta impurities can substitute Zn atoms and act as donor impurities in the host semiconductor.

1. Introduction

Zinc oxide is a multifunctional semiconductor considered as a promising candidate for many technological applications [1,2]. In addition to its chemical and thermal stability, abundance and low cost, its attractive remains in the possibility of changing its structural, electronic and magnetic properties by doping it. Because of the emergent properties that arise with doping, this compound is investigated for applications in solar cells, gas sensors, transparent electrodes, catalysts, light emitting diodes, and laser devices [3–9].

Among the wide variety of production methods, the sol-gel processes have been investigated in order to synthesize pure and doped ZnO powders. In general, these kind of bottom-up approaches are simple mechanisms for preparing different nanometric structures. In this respect, research on nanostructured pure and doped ZnO synthesized by sol-gel methods has gained attention in the last years [2,10–13]

In this work, we present a study of the synthesis of tantalum-doped ZnO prepared by the sol-gel method via the acetate route. The synthesis and growth of Ta-doped ZnO nanoparticles by different ways is a subject of current interest due to the structural, electrical and other properties that appear with the inclusion of the Ta impurity [14,15], with most of the investigations being done on thin films [16–19]. The diversity of reported chemical and physical methods to produce the doped ZnO also indicates the interest on finding a simple way to obtain it. In this respect, different sol-gel acetate routes are good candidates that satisfy this requirement, and have proven to successfully synthesize pure and doped oxides [20–23]. So, following this concept, this paper focuses on synthesizing Ta-doped ZnO by an easy sol-gel acetate route. Using X-ray diffraction (XRD) and micro-Raman, UV–visible, and impedance spectroscopies, we experimentally study pure and Ta-doped ZnO. XRD and Raman measurements allow a detailed analysis of the involved crystal structures and their evolution with annealing treatments. In particular, we performed a simultaneous monitoring of the crystallite growth and the Ta doping process of the wurtzite ZnO host structure. In addition, we use impedance and UV–visible spectroscopies to investigate the role of Ta doping on the electrical and optical properties of the samples. All these experimental measurements are also complemented with own first principles calculations. The computational modeling allows us controlling the impurity location in the host structure, and analyzing how its inclusion modifies the structural, vibrational and electronic properties of the oxide. In this respect, various

* Correspondence to: Departamento de Física and Instituto de Física La Plata (IFLP, CONICET), Facultad de Ciencias Exactas, Universidad Nacional de La Plata, CC 67, 1900 La Plata, Argentina.
E-mail address: richard@fisica.unlp.edu.ar (D. Richard).

http://dx.doi.org/10.1016/j.ceramint.2017.09.232
Received 8 August 2017; Accepted 29 September 2017
Available online 30 September 2017

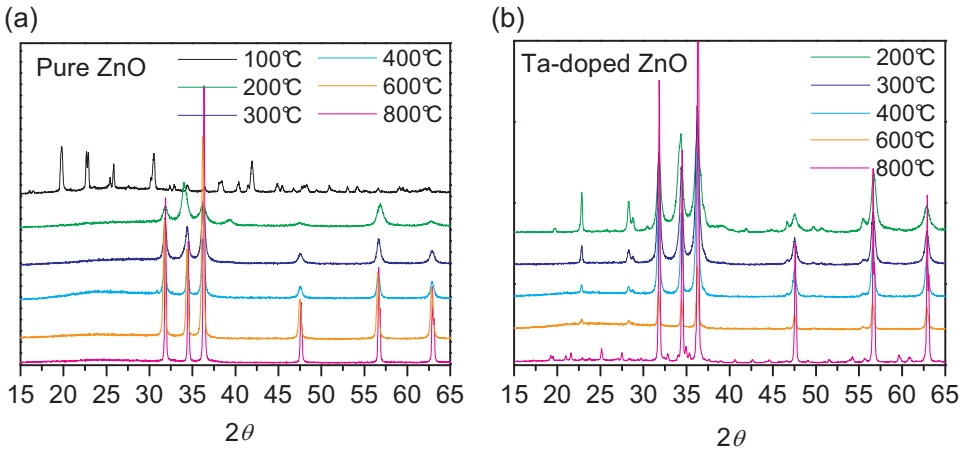

Fig. 1. XRD patterns for (a) pure ZnO and (b) Ta-doped ZnO.

ab initio calculation approaches have been applied to study some of these properties in pure and doped ZnO (see for example Refs. [24–31].). Nevertheless, none of these first principles investigations focused on studying in detail the case of Ta-doped ZnO.

So, to the best of our knowledge, we present for the first time a study for Ta-doped ZnO synthesized by the sol-gel acetate route. Also, this is the first time all the above mentioned properties of this compound are investigated by combining experimental techniques and first principles methods.

2. Methodology

2.1. Sample preparation

Zinc acetate dihydrate (ZAD), $Zn(CH_3COO)_2{\cdot}2H_2O$ (Baker), and tantalum oxide, Ta_2O_5 (Aldrich), were used as precursors to synthesize Ta-doped ZnO. All reagents were of analytical grade and were used without any further purification. In order to reach 3 at% Ta doping in ZnO, we dissolved 6 g of ZAD in 125 ml of 2-propanol, and 186 mg of Ta_2O_5 in 50 ml of glacial acetic acid. Both solutions were mixed and magnetically stirred in a heating plate at 100 °C until drying. A pure ZnO reference sample were simultaneously synthesized using the same procedure, but without the Ta_2O_5 precursor.

The obtained powders (pure and doped cases) were fractionated and placed into crucibles, and each of them was thermally treated for 2 h at T_t = 200, 300, 400, 600 or 800 °C in a muffle furnace without any special atmospheric condition.

2.2. Instrumentation

The resulting samples were characterized at room temperature by XRD, micro-Raman spectroscopy, and impedance spectroscopy. The phase evolution with the different thermal treatments was studied by XRD (Rigaku Ultima IV, Cu Kα radiation) and micro-Raman spectroscopy (WITec Alpha300RA, λ = 532 nm).

For the pure and doped powders treated at T_t = 600 °C we performed UV–visible (Shimadzu UV-2600 spectrometer) and impedance (Gamry Inst. Ref. 3000) spectroscopy measurements. To obtain the impedance spectra, after the thermal treatment the powders were pressed at 40 MPa into pellets of ½ in diameter, and sintered at 600 °C for 10 h. The resulting pellets were about 3 mm thickness. Impedance spectra in the range 10 Hz–1 MHz were measured using stainless steel electrodes, and different DC bias between 1 and 8 V.

2.3. Computational procedure

We performed ab initio calculations by means of the Density Functional Theory (DFT) [32,33]. The calculations were made using the Vienna ab initio Simulation Package (VASP) code [34–37], with the Generalized Gradient Approximation (GGA) exchange-correlation functional, using the Perdew-Burke-Ernzerhof (PBE) parameterization [38,39]. We used the Projector Augmented-Wave (PAW) potentials with the following valence electrons: Zn ($3d^{10}$ $4s^2$), O ($2s^2$ $2p^4$) and Ta ($5p^6 5d^3 6s^2$). In the case of ZnO we utilized the pristine unit cell of the wurtzite hexagonal phase (h-ZnO), and in the case of Ta-doped ZnO we build a 2 × 2 × 2 supercell and thus substituting a Zn atom with a Ta atom. By performing this atomic substitution we reach the $Ta_{1/8}Zn_{7/8}O$ structural formula, i.e., 12.5 at% of Ta doping. A *k*-space grid of 6 × 6 × 6 was selected in all the calculations and a cut-off energy for the plane wave expansion of 400 eV. The structures were optimized until the forces in all the atoms were lower than 0.01 eV/Å, and the unit cell was optimized until the components of the stress tensor were lower than 1 kBar. After that, we proceed with the vibrational analysis, utilizing the Phonopy code for the phonons calculations [40]. Finally, we applied the Porezag & Pederson methodology [41], as implemented in the *vasp_raman.py* script [42], to determine the polarizability of every single eigenvector of the Γ-point phonons in order to get the simulated off-resonant Raman spectra.

3. Results

3.1. XRD

In Fig. 1a we present the XRD patterns of pure ZnO powders after the different thermal treatments. The initial pattern (after the drying at 100 °C) can be indexed to the structure of anhydrous zinc acetate (PDF card number 000-21-1467) [43]. Thermal treatments at higher temperatures promote the formation of the ZnO wurtzite structure (h-ZnO, group 186), which is characterized by the three major peaks in the range 2θ = 32–37°. In addition, for the treatments at T_t = 200–300 °C we found also the cubic ZnO phase (c-ZnO, group 216), whose main peaks are at 2θ = 39° and 2θ = 34°. For T_t > 300 °C, only those peaks corresponding to h-ZnO are observed, indicating that the synthesized oxide has high purity.

In Fig. 1b we show the XRD patterns corresponding to the series of Ta-doped ZnO. These patterns present the same features that those corresponding to the pure ZnO samples, with two main differences. First, we observe the presence of Ta_2O_5 precursor phase after any thermal treatment. This phase has its principal peak at 2θ = 23°, and its contribution to the XRD pattern decreases as T_t increases, being minimum after the 600 °C treatment. On the other hand, after the treatment at 800 °C new diffraction peaks appear, which correspond to a third phase, associated to the formation of the $ZnTa_2O_6$ mixed oxide (whose pattern is indexed with PDF number 000-49-0746). Regarding the h-ZnO phase, its diffraction peaks become sharper and narrow with

Table 1
Lattice parameters and crystallite size for pure and Ta-doped h-ZnO phases.

	Pure h-ZnO			Ta-doped h-ZnO			
T_t (°C)	a (Å)	c (Å)	D (nm)	a (Å)	c (Å)	D (nm)	x_r
200	3.2571(1)	5.238(1)	13.1(3)	3.2465(2)	5.2239(4)	18.1(2)	0.0060
300	3.2513(3)	5.2182(6)	23.5(2)	3.25001(2)	5.2148(3)	27.0(2)	0.0175
400	3.2529(3)	5.2139(5)	30.9(3)	3.2521(2)	5.2129(3)	33.9(2)	0.0225
600	3.2532(2)	5.2124(3)	52.0(7)	3.2533(2)	5.2117(3)	55.4(6)	0.0174
800	3.25143(9)	5.2094(1)	124(1)	3.2500(1)	5.2066(2)	132(2)	–

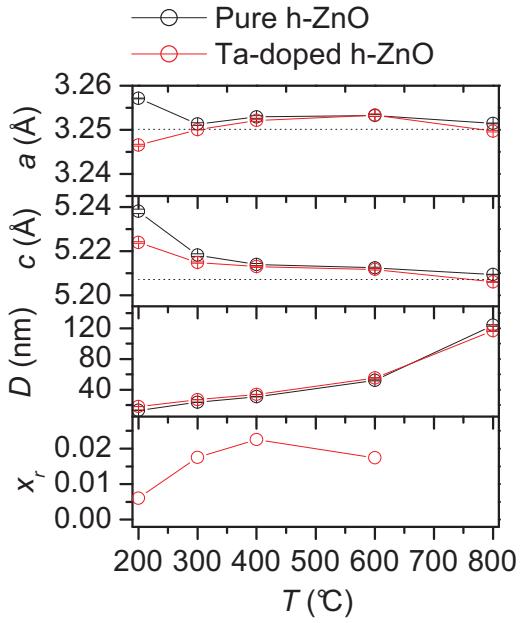

Fig. 2. Lattice parameters, crystallite size, and effective Ta doping determined from Rietveld refinement (see text). The dotted line stands for the reference value of Kisi et al. [46].

increasing T_t, which indicates a more complete crystallization of the Ta-doped ZnO structure.

For the pure and Ta-doped powders we analyzed the h-ZnO phase evolution by Rietveld refinement of the crystal structure [44]. In Table 1 and Fig. 2 we present in each case the obtained lattice parameters, a and c, and crystallite size, D. We found that for both, pure and Ta-doped samples, D increases from 13 to about 130 nm in the considered temperature range for T_t. We observe that D increases its growth rate for the treatments above 600 °C (see Fig. 2), which is in very good agreement with the previous results for pure ZnO formation during thermal decomposition of zinc acetate [45]. In addition, the obtained lattice parameters evolve with T_t toward those reported for undoped h-ZnO powder (a = 3.2501(1) Å, c = 5.2071(1) Å [46]) (see Fig. 2).

In the case of Ta-doped ZnO, from the Rietveld refinement we also determined the effective doping x_r for $Zn_{1-xr}OTa_{xr}$ in the hexagonal phase. To this purpose we suppose that the samples only present crystalline phases, and are those observed in the XRD patterns. So, based on the used initial amounts of Zn and Ta and the fitted Rietveld weight fractions, we calculated x_r. We found that after the treatments at 400–600 °C we reach about 2 at% Ta doping (see Table 1 and Fig. 2). In the case of the powder treated at 800 °C we did not determine x_r due to the complexity of the XRD pattern with the presence of the $ZnTa_2O_6$ secondary phase.

3.2. micro-Raman spectroscopy

The room temperature non-resonant Raman spectra for pure and Ta-doped ZnO are presented in Fig. 3a and b, respectively. In the case of pure ZnO, we found that these spectra evolve from the anhydrous zinc acetate spectrum to that corresponding to h-ZnO (see Fig. 3a). Initially, for the powder prepared at 100 °C, we found all Raman modes of zinc acetate, with a main peak at 959 cm^{-1} assigned to ν(C–C) stretching mode [47]. This initial spectrum also presents organic ν(C–H) stretching modes near 3000 cm^{-1} (not shown in Fig. 3a), which disappear after any thermal treatment. After treatments at T_t = 300–400 °C, the spectra exhibit a high fluorescence signal that makes quite difficult to follow the evolution of the Raman modes. For T_t > 400 °C the spectra present the typical Raman features of h-ZnO. In this sense, we found a main band at 440 cm^{-1}, followed by bands at 101, 333 and 382 cm^{-1}. These modes correspond to E_2(high), E_2(low), second order E_2(high)-E_2(low), and A_1(TO) phonon modes, respectively [10,47,48]. We observe that for the most prominent peak at 440 cm^{-1} there is a slight shift to higher frequencies as T_t increases (blueshift), which suggest a compressive strain in the lattice parameters. In addition, the peak width diminishes with increasing T_t, in agreement with the crystallinity increase already observed by XRD.

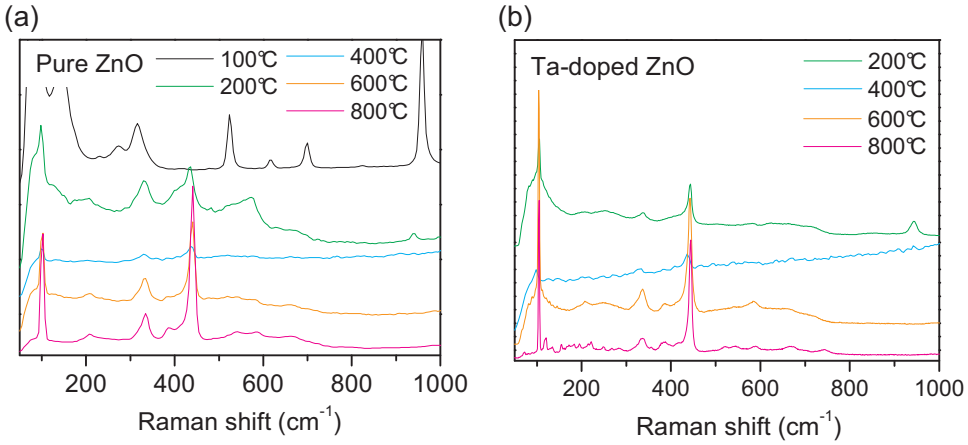

Fig. 3. Raman spectra for (a) pure ZnO and (b) Ta-doped ZnO.

On the other hand, the Raman spectra for Ta-doped ZnO evolve with T_t in a similar way to those of pure ZnO (see Fig. 3b). For $T_t > 400$ °C, the presence of the same phonon modes than those observed for the pure samples suggests that in these cases Ta impurities enter in the h-ZnO host lattice without producing significant changes to the structure. However, when we compare these spectra with those corresponding to the pure ZnO series, we found a slightly more pronounced peak at 382 cm^{-1}. As can be seen in Fig. 3b, for $T_t > 400$ °C we found that the Ta-doped h-ZnO phase also presents a E_2(high)/E_2(low) intensity ratio lower than unity, which is inverse to that observed in the pure ZnO samples. This ratio inversion could be associated with the Ta doping of the hexagonal phase, a hypothesis that is supported if we focus on the sample treated at 600 °C, where no additional modes to those of h-ZnO are observed (i.e., we do not detect an additional phase that could affect the intensity of the considered peaks).

Finally, after the thermal treatment at 800 °C we observe the presence of many additional minor modes to those of h-ZnO, especially in the range 150–300 cm^{-1}, but also in the 500–800 cm^{-1} range. Considering our previous XRD results, we speculate that these modes correspond to the $ZnTa_2O_6$ phase occurrence. Confocal Raman mapping allows the study of the phase distribution in the samples at the microscopic level. To this purpose, for T_t = 800 °C we chose the 440 and 740 cm^{-1} peaks as references for the h-ZnO and $ZnTa_2O_6$ phases, respectively. In Fig. 4 we present the 2D Raman image generated by integration of these, and their corresponding spectra. We found that at T_t = 800 °C, the $ZnTa_2O_6$ phase appeared as a segregate (indicated in blue color in Fig. 4a), as also evidenced by XRD Rietveld analysis, probably as a consequence of tantalum loss from the Ta-doped h-ZnO phase.

Regarding the detection of the Ta_2O_5 phase through Raman spectroscopy, we did not find any significant contribution of this oxide to the spectra. To check this we performed additional measurements using thermally treated Ta_2O_5 powder, and we confirmed that this oxide does not contribute to the spectrum with any peak of those observed for the Ta-doped ZnO samples. Regarding this, the Ta_2O_5 powder spectra are practically the same to those already presented for Ta_2O_3 coatings in Ref [49].

3.3. UV–visible spectroscopy

Diffuse reflectance spectra for pure and Ta-doped ZnO are shown in Fig. 5a. These spectra correspond to samples thermally treated at T_t = 600 °C, as mentioned above. As can be seen, there is practically no difference in $R(\lambda)$ between these two cases. For both samples, it is quite clear that reduction in reflectance starts at about 460 nm.

In Fig. 5b we present these spectra after the Kubelka-Munk treatment, considering a direct allowed transition [50]. In each case, the band gap energy E_g is obtained from the intersection point between the horizontal $h\nu$ axis and the tangent line to the point of inflection of the curve. By using this method we obtained the values indicated by arrows in Fig. 5b, E_g = 3.26(1) and 3.27(1) eV for pure and Ta-doped ZnO, respectively. So, any change in E_g with Ta doping is at the edge of the precision limit of this experimental method. Nevertheless, our results are in good agreement with those reported in other similar Ta-doped samples. Previous measurements of E_g in Ta-doped ZnO show dissimilar results, and suggest that the E_g behavior with Ta concentration depends on the considered preparation method for the sample. In this sense, according to the absorption data on nanocrystals reported by Kong et al., E_g increases from 3.19 to 3.34 eV when Ta doping ranges from 0 to 4 at%, respectively [14]. In the same way, later measurements for thin film samples presented similar increases in E_g when consider the same Ta doping range [17,19,51]. However, also for Ta-doped ZnO films Ravichandran et al. found E_g values that practically do not change with doping concentration [18]. But in this respect, the investigations of Cao *et al.* and also those of Mahmood et al. demonstrate that the sample annealing temperatures could affect the measured value of E_g [16,17], a fact that we consider explains the differences in E_g mentioned earlier.

3.4. Impedance spectroscopy

In Fig. 6a and b we present the Nyquist plots of both pure and Ta-doped ZnO samples for the different operation DC bias voltage. In both cases, only a portion of a semicircle-like branch is seen, with its origin on the real axis. In general, at high frequencies, for low values of the real part of the impedance, the plots practically do not change as the bias voltage varies. On the other hand, at lower frequencies, for higher values of Z_{real}, the DC bias modifies the open arc part of the Nyquist plot. This effect is clear in the case of pure ZnO, where as DC bias increases the arc increases its final slope (Fig. 6a).

Our data were analyzed by fitting to the equivalent electrical circuit model of Fig. 6c. This model is a series-parallel combination circuit, where each resistance is in parallel with a constant phase element (CPE), and each parallel contacted R-CPE pair stands for the grain interiors and grain boundary contribution to the total impedance. A CPE represents a non-ideal capacitor, and its impedance can be expressed as

$$Z_{CPE} = \frac{1}{(j\omega)^{\alpha} Y_0},$$

where Y_0 is the capacitance, and α is an exponent equaling unity in case of an ideal capacitor.

The solid lines in the Nyquist plots of Fig. 6 are the least-squares fits of our model to the corresponding impedance data. The obtained contributions to the total impedance are plotted against the DC bias voltage in Fig. 7. We called R_{gi} and R_{gb} the resistance for the grain interiors and grain boundary, respectively. Considering the pellet diameter and thickness, we calculated the corresponding resistivities ρ_{gi} and ρ_{gb}. In Fig. 7 such values are indicated on the right axis of each resistance plot.

For the pure ZnO, R_{gi} is one order of magnitude lower than R_{gb}. The

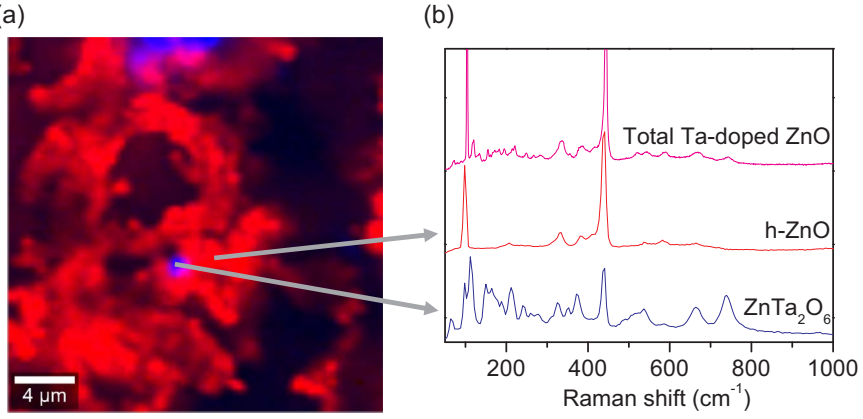

Fig. 4. (a) 2D Raman mapping of the Ta-doped ZnO sample treated at 800 °C considering the 440 and 740 cm^{-1} peaks (in red and blue, respectively), and (b) their corresponding h-ZnO and $ZnTa_2O_6$ Raman spectra extracted from the points indicated by arrows. The *y*-axis in (b) has a different scale for each spectrum to get a better visualization.

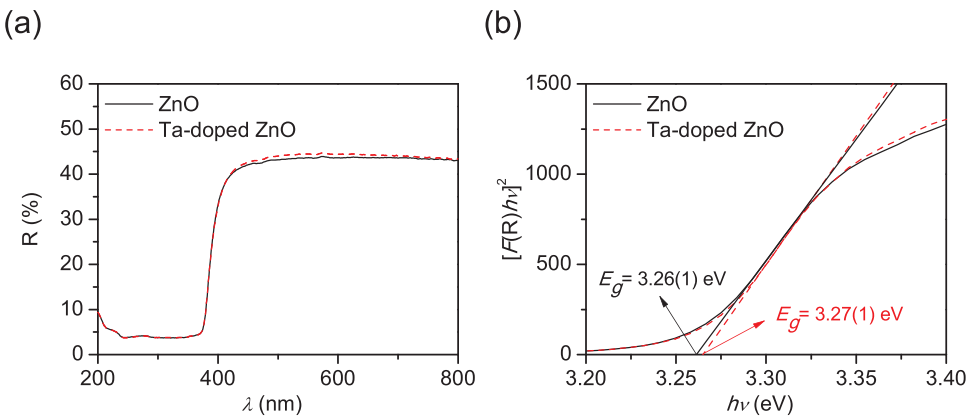

Fig. 5. (a) Diffuse reflectance spectra for pure and Ta-doped ZnO, and (b) their corresponding Kubelka-Munk transformed reflectance spectra.

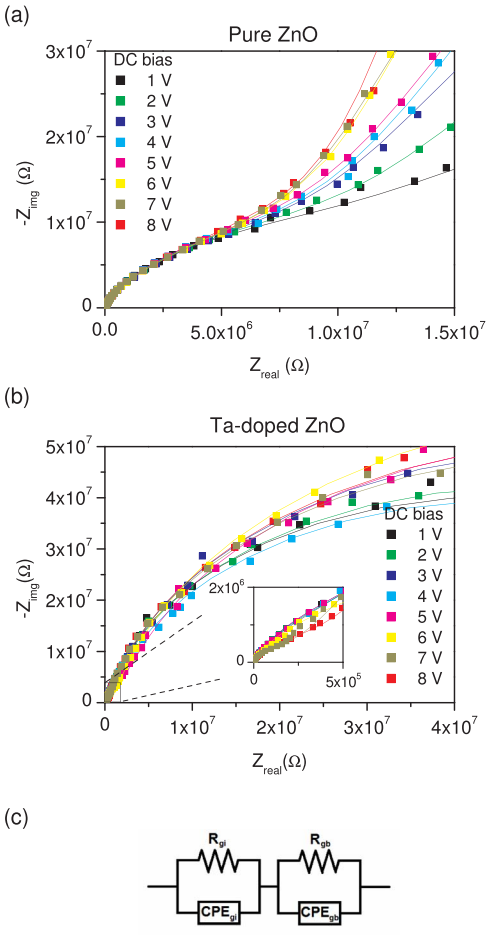

Fig. 6. Nyquist plots for (a) pure ZnO and (b) Ta-doped ZnO, and (c) proposed equivalent circuit.

assignments of the R_{gi} and R_{gb} parameters were chosen according to previous works [52–54]. As can be seen in Fig. 7, R_{gb} monotonously increases with DC bias. This dependence is a consequence of the open arc part behavior with bias voltage already described for Fig. 6a. For the Ta-doped sample we also found that R_{gi} is one or two orders of magnitude lower than R_{gb}. In addition, we observe that for DC bias ranging from 1 to 6 V R_{gi} is about 1 MΩ, while for higher bias it abruptly falls to about 0.2 MΩ, which is an effect of the change in the starting curvature of the Nyquist plot observed for these DC bias values (see Fig. 6b, inset plot).

On the other hand, for both samples the CPE impedances are characterized by α value near unity over all the considered DC bias range, and a Y_0 capacitance in the range 30–200 Ss^{α}.

When we compare the resistances of both pure ZnO and Ta-doped ZnO, it becomes clear that the R_{gi} and R_{gb} values in the doped system are lower to those corresponding to the pure case. This result suggests that Ta doping modifies both grain interiors and boundary, diminishing their resistivities, in overall good agreement with the nominal triple-donor character of the Ta atom (element with valence 5 +) when acts as substitutional impurity in the $Zn^{2+}O^{2-}$ host structure. In this sense, when the Ta atom locates at a regular Zn site, it donates negative charge, which enhances the electrical conduction. Also, since the concentration of Ta impurities is lower in the grain boundary than in its interiors, it is expected the more pronounced diminishing of R_{gi} than R_{gb} with Ta doping. In this sense, R_{gi} changes from 9 to 10 MΩ to 0.2–1.1 MΩ with Ta doping (*i.e.*, a mean decrease to about 7% of the undoped sample values), while R_{gb} diminishes from 84 to 910 MΩ to 90–134 MΩ (*i.e.*, a decrease to about 20%).

3.5. Computational simulations

In order to obtain the Raman spectra from first principles, we first calculate the equilibrium geometrical structure for pure h-ZnO and Ta-doped h-ZnO. The obtained cell lattice parameters are: $a = b = 3.254$ Å and $c = 5.251$ Å for h-ZnO, and $a = b = 3.251$ Å and $c = 5.209$ Å for Ta-doped h-ZnO (expressed in terms of the pristine h-ZnO unit cell). As can be observed, Ta doping induces a compressive strain in the structure, lowering the values of the cell lattice parameters. This result can be considered a consequence of the change of the involved ionic radii with the cation substitution [55]. In effect, we can also look the local structure modification obtained with the inclusion of the Ta impurities. According to our calculations, when we allow the relaxation of the internal atomic positions the Ta-O final distances $d_{Ta\text{-}O}$ take values in the range 1.90–2.00 Å, which tend to be lower than the original $d_{Zn\text{-}O} = 1.98$ Å for pristine h-ZnO.

When we compare these structural results with those obtained by XRD, we found that there exists a good correspondence between the predicted compressive strain introduced by Ta doping and the experimental slight diminishing of the h-ZnO phase lattice parameters obtained with the Ta doping (see Table 1). Considering that theoretically we deal with a higher at% of Ta doping of the host structure, it is expected that the predicted structural effects with doping should be more pronounced than in experiments.

The vibrational spectra are analyzed first in terms of the partial density of phononic sates (phonon DOS), presented in Fig. 8. For h-ZnO, the phonon density of states shows the typical two regions, the first from 0 to 250 cm^{-1} with a major contribution for Zn in comparison to O, and the second one from 350 to 550 cm^{-1} majorly contributed from O in comparison to Zn. The Ta-doped h-ZnO case shows a broader phonon spectrum, as expected from the symmetry breaking introduced by the Ta doping. The contribution from this atom is mainly localized in

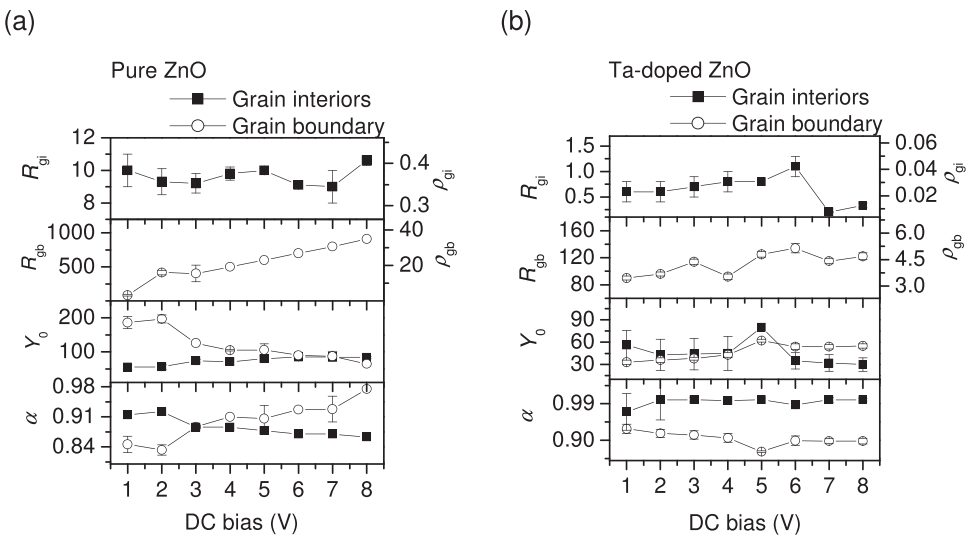

Fig. 7. Fitted parameters for the proposed equivalent circuit in (a) pure ZnO and (b) Ta-doped ZnO. R_{gi} and R_{gb} are in units of MΩ, and Y_0 in units of 10^{-12} Ss^{α}. We also indicate the corresponding values for resistivities ρ_{gi} and ρ_{gb} on the right, in units of MΩm.

the region of 0–300 cm^{-1}, as expected for this relatively higher mass and with an additional small contribution at 650 cm^{-1}.

After this vibrational analysis, we followed with the calculation of the off-resonance Raman spectra for both structures. The corresponding results are shown in Fig. 9. In the case of h-ZnO, we obtain the expected Raman modes B_1, E_2(high), E_1, A_1, and E_2(low) at 534, 433, 395, 375 and 95 cm^{-1}, respectively (see Fig. 9a and b). These Raman shift values are in very good correspondence with those determined experimentally with some differences in their relative intensities (see Fig. 3a). Regarding the intense B_1 mode, if we allow LO/TO splitting this mode could be shifted to lower values. However, LO/TO splitting has not been considered in the present calculations. When we compare the calculated h-ZnO Raman spectrum with that predicted for Ta-doped h-ZnO, we found that Ta doping introduces additional peaks with important contribution for the Raman cross section (see Fig. 9c). Among them, we can distinguish the peaks located at 180, 280, 474, 497, 523 and 650 cm^{-1}. In most of these cases, there is a relevant contribution from Ta atoms, as schematized in the corresponding Fig. 9d, demonstrating how the presence of Ta doping can be evidenced from the Raman analysis.

In reference to the electronic structure, in Fig. 10 we present the calculated densities of electronic states (DOS). For pure h-ZnO we can distinguish a valence band separated by about 1 eV from the conduction band. This result subestimates the experimental value of the forbidden band gap energy (E_g is about 3.2 eV according to our measurements and previous results [14,17–19]), as it is well known for GGA-PBE calculations. Nevertheless, we can still do the comparison between the pure and doped system, just in relative terms. For our case, the Ta doping introduces electronic levels at the Fermi energy of the ZnO bulk host, thus generating a semi metallic situation (see Fig. 10b). Also, despite the fact that GGA-PBE calculations subestimate the E_g values, according to our PAW calculations the inclusion of the Ta impurity diminishes E_g in about 0.3 eV due to the presence the donor levels. A change in E_g of this order of magnitude has not been experimentally observed, as can be seen from our UV–visible measurements and other experimental results reported for Ta-doped ZnO [14,17–19]. However, it is worth to notice that this effect of the Ta atom on the E_g value could be due to the high Ta doping considered in our calculations. For example, it has been already observed by first principles that for larger Ta-doped ZnO supercells (i.e., a lower Ta impurity concentration) the donor levels introduced by the impurity lie on the conduction band bottom [24]. So, in such cases the presence of the Ta impurity does not modify the predicted value of E_g, which is a prediction in better agreement with our UV–visible measurements for E_g.

4. Discussion and conclusions

The XRD and Raman results presented for the reference sample synthesized without the Ta_2O_5 precursor show that the initial solution dehydrates first into anhydrous zinc acetate, and evolves to h-ZnO as the thermal treatment temperature increases. During this evolution, the hexagonal phase coexists with the cubic one after treatments in the range 200–300 °C. The presented phase transitions and the crystallite size growth rate for h-ZnO are consistent with those previously reported for undoped ZnO synthesized by other methods [45,47,56]. On the other hand, for the Ta-doped ZnO samples we found similar crystal structure results to those of pure ZnO, for both the hexagonal phase lattice parameters and the crystallite size evolution with the different

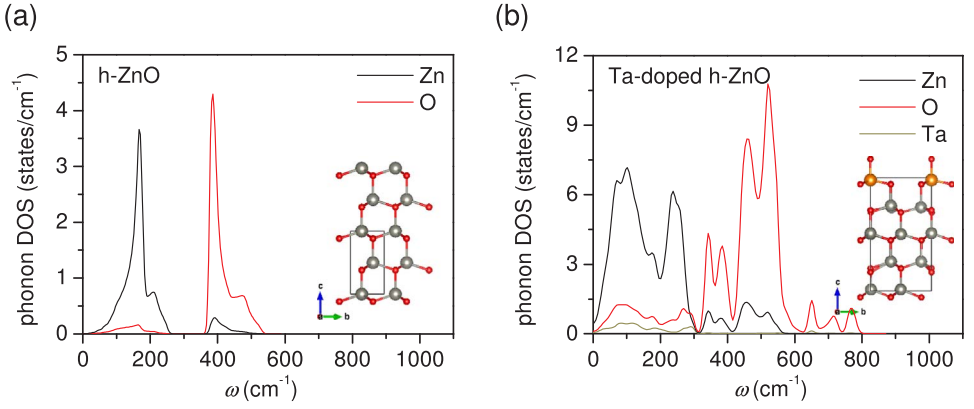

Fig. 8. Total and partial density of phononic states for (a) h-ZnO and (b) Ta-doped h-ZnO. The insets show the corresponding used cells. Grey, red and orange spheres stand for Zn, O, and Ta atoms, respectively.

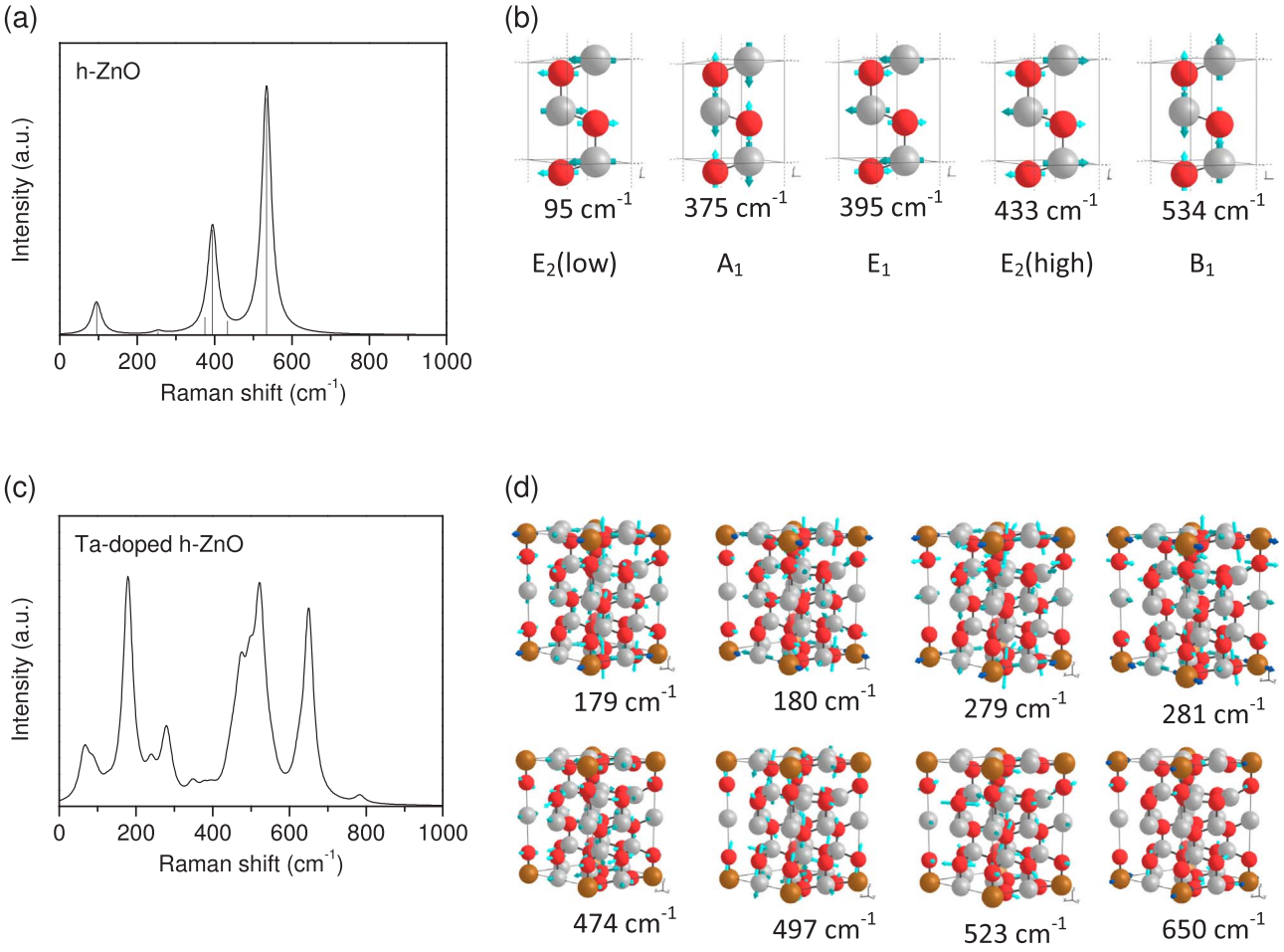

Fig. 9. Off resonance theoretical Raman spectra for (a) h-ZnO and (c) Ta-doped h-ZnO, and (b, d) vibrational representations for selected modes.

thermal treatments. However, we observed that the low Ta doping slightly diminishes the lattice parameters of the unit cell, which can be expected according to our first principles calculations of the equilibrium structures of pure and Ta-doped h-ZnO. After the treatment at 600 °C we reached an optimal situation in which the sample is highly crystalline, the formation of hexagonal phase is maximum, and the Ta doping is about 2 at%. Later, after the treatment at 800 °C we found that the mixed oxide $ZnTa_2O_6$ is segregated, in a low temperature modification of its orthorhombic form. In this sense, it has been reported using solid-state or other sol-gel methods that for thermal treatments in the range 650–1100 °C the formation of $ZnTa_2O_6$ is promoted [57,58].

In order to study the optical and electrical properties of Ta-doped ZnO, and considering the preceding results, we performed UV–visible and impedance spectroscopy measurements for powders calcined at 600 °C (in form of pellets for impedance studies). In this respect, our results show that the achieved Ta doping does not modify the E_g value. In addition, the semiconductor resistivity in the Ta-doped sample is lower than that of the pure sample, in agreement with the donor character of the Ta impurity in the ZnO host structure. We found that Ta doping produces a more pronounced decrease in the grain interiors contribution to the impedance compared to the grain boundary contribution. At this point, it is important to mention that both pure and Ta-doped samples present practically the same crystallite size, as

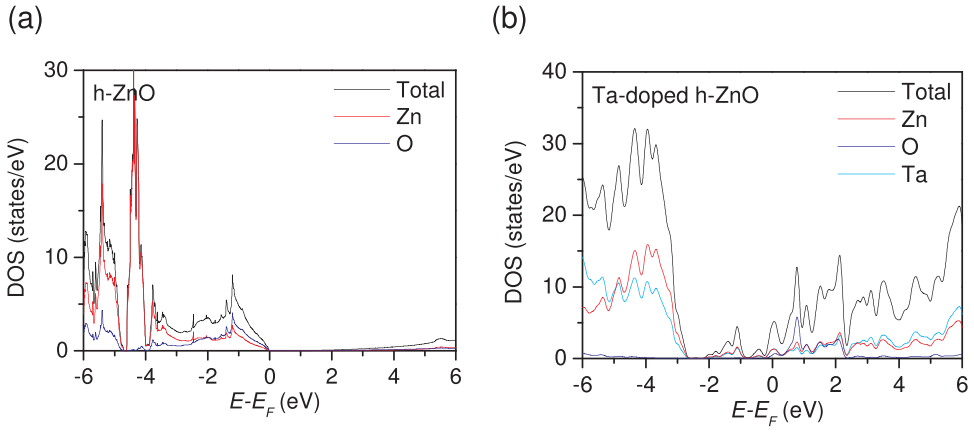

Fig. 10. Total and partial DOS for (a) h-ZnO and (b) Ta-doped h-ZnO.

observed by XRD. So, the diminishing of the resistivity may be indeed produced by Ta doping. Although this is the first time where impedance spectroscopy measurements are presented for Ta-doped ZnO, previous work has shown similar behavior for the total resistivity when the host matrix is doped with Ta. Concerning this, it has been showed that when ZnO films are doped with 1–2 at% Ta, the total resistivity decreases about one order of magnitude [17,18]. On the other hand, impedance spectra has been applied to the study of ZnO doped with other impurities, with results that follow the same trend to that presented in this work. For example, Zhou et al. measured a decrease of one order of magnitude for the resistivity when ZnO is doped with trivalent Al impurities. Also, in an opposite way, acceptor impurities increase the sample resistivity [59].

In summary, in this work we performed a detailed study for the first time of the sol-gel method in acetic medium for synthesizing Ta-doped ZnO. By using different experimental techniques, we followed the crystallization evolution towards the h-ZnO phase, together with the Ta doping process of the crystal structure. We demonstrate that the maximum formation of Ta-doped h-ZnO is reached after heating the sample at 400–600 °C. For the doped oxide, the inclusion of the Ta impurity in the host structure is accompanied by a decrease in both grain interiors and grain boundary resistivities, in agreement with the donor character of the dopant. The theoretical simulations allow us to confirm the Ta doping on the h-ZnO host, explaining the reduction of the resistivity in the doped samples.

Acknowledgments

The authors wish to thank the Uruguayan CSIC, ANII and PEDECIBA funding institutions. We would also like to thank financial support of EQC-X-2012-1-14 research project. D. R. wishes to thank to Agencia Nacional de Investigación e Innovación (ANII) for providing the opportunity to undertake this research by supporting her Post-doc “Fondo Profesor Dr. Roberto Caldeyro Barcia” (code PD_NAC_2015_1_108453), and also wishes to thank all the personnel of Facultad de Química (UdelaR) for their hospitality during his stay. D. R. is member of CONICET, Argentina.

References

[1] Ü. Özgür, Ya.I. Alivov, C. Liu, A. Teke, M.A. Reshchikov, S. Doğan, V. Avrutin, S.-J. Cho, H. Morkoç, A comprehensive review of ZnO materials and devices, J. Appl. Phys. 98 (2005) 041301, http://dx.doi.org/10.1063/1.1992666.

[2] A. Kolodziejczak-Radzimska, T. Jesionowski, Zinc oxide – from synthesis to application: a review, Materials 7 (2014) 2833, http://dx.doi.org/10.3390/ma7042833.

[3] S.-D. Baek, P. Biswas, J.-W. Kim, Y.C. Kim, T.I. Lee, J.-M. Myoung, Low-temperature facile synthesis of Sb-doped p-type ZnO nanodisks and its application in homojunction light-emitting diode, ACS Appl. Mater. Interfaces 8 (2016) 13018–13026, http://dx.doi.org/10.1021/acsami.6b03258.

[4] S.B. Bashar, M. Suja, M. Morshed, F. Gao, J. Liu, An Sb-doped p-type ZnO nanowire based random laser diode, Nanotechnology 27 (2016) 065204, http://dx.doi.org/10.1088/0957-4484/27/6/065204.

[5] K.G. Girija, K. Somasundaram, A. Topkar, R.K. Vatsa, Highly selective H_2S gas sensor based on Cu-doped ZnO nanocrystalline films deposited by RF magnetron sputtering of powder target, J. Alloy. Compd. 684 (2016) 15–20, http://dx.doi.org/10.1016/j.jallcom.2016.05.125.

[6] K.M. Lee, C.W. Lai, K.S. Ngai, J.C. Juan, Recent developments of zinc oxide based photocatalyst in water treatment technology: a review, Water Res. 88 (428–448) (2016) 0043–1354, http://dx.doi.org/10.1016/j.watres.2015.09.045.

[7] D. Sengupta, P. Das, B. Mondal, K. Mukherjee, Effects of doping, morphology and film-thickness of photo-anode materials for dye sensitized solar cell application – a review, Renew. Sustain. Energy Rev. 60 (2016) 356–376, http://dx.doi.org/10.1016/j.rser.2016.01.104.

[8] C. Tong, J.-H. Yun, Y.-J. Chen, D. Ji, Q. Gan, W. Anderson, Thermally dDiffused Al:ZnO thin films for broadband transparent conductor, ACS Appl. Mater. Interfaces 8 (2016) 3985–3991, http://dx.doi.org/10.1021/acsami.5b11285.

[9] Y. Al-Hadeethi, A. Umar, A.A. Ibrahim, S.H. Al-Heniti, R. Kumar, S. Baskoutas, Bahaaudin M. Raffah, Synthesis, characterization and acetone gas sensing applications of Ag-doped ZnO nanoneedles, Ceram. Int. 43 (2017) 6765–6770, http://dx.doi.org/10.1016/j.ceramint.2017.02.088.

[10] A.K. Ojha, M. Srivastava, S. Kumar, R. Hassanein, J. Singh, M.K. Singh, A. Materny, Influence of crystal size on the electron–phonon coupling in ZnO nanocrystals investigated by Raman spectroscopy, Vib. Spectrosc. 72 (2014) 90–96, http://dx.doi.org/10.1016/j.vibspec.2014.02.013.

[11] M.K. Lima, D.M. Fernandes, M.F. Silva, M.L. Baesso, A.M. Neto, G. Rodriguês de Morais, C.V. Nakamura, A. de Oliveira Caleare, A.A. Winkler Hechenleitner, E.A. Gómez Pineda, Co-doped ZnO nanoparticles synthesized by an adapted sol-gel method: effects on the structural, optical, photocatalytic and antibacterial properties, J. Sol-Gel Sci. Technol. 72 (2014) 301, http://dx.doi.org/10.1007/s10971-014-3310-z.

[12] M. Hjiri, L. El Mir, S.G. Leonardi, A. Pistone, L. Mavilia, G. Neri, Al-doped ZnO for highly sensitive CO gas sensors, Sens. Actuators B 196 (2014) 413–420, http://dx.doi.org/10.1016/j.snb.2014.01.068.

[13] B. Khodadadi, M. Bordbar, A. Yeganeh-Faal, Optical, structural, and photocatalytic properties of Cd-doped ZnO powders prepared via sol-gel method, J. Sol-Gel Sci. Technol. 77 (2016) 521–527, http://dx.doi.org/10.1007/s10971-015-3877-z.

[14] J.-Z. Kong, A.-D. Li, H.-F. Zhai, Y.-P. Gong, H. Li, D. Wu, Preparation, characterization of the Ta-doped ZnO nanoparticles and their photocatalytic activity under visible-light illumination, J. Solid State Chem. 182 (2009) 2061–2067, http://dx.doi.org/10.1016/j.jssc.2009.03.022.

[15] B.-L. Guo, P. Han, L.-C. Guo, Y.-Q. Cao, A.-D. Li, J.-Z. Kong, H.-F. Zhai, D. Wu, The antibacterial activity of Ta-doped ZnO nanoparticles, Nanoscale Res. Lett. 10 (2015) 336, http://dx.doi.org/10.1186/s11671-015-1047-4.

[16] F. Cao, Y.-D. Wang, J.-Z. Yin, M.-L. Cong, L.-Y. Han, Influence of post-annealing temperature on properties of Ta-doped ZnO transparent conductive films, Chin. Phys. Lett. 26 (2009) 114203, http://dx.doi.org/10.1088/0256-307X/26/11/114203.

[17] K. Mahmood, D. Song, S. Bin Park, Effects of thermal treatment on the characteristics of boron and tantalum-doped ZnO thin films deposited by the electrospraying method at atmospheric pressure, Surf. Coat. Technol. 206 (2012) 4730–4740, http://dx.doi.org/10.1016/j.surfcoat.2012.01.047.

[18] K. Ravichandran, K. Subha, N. Dineshbabu, A. Manivasaham, Enhancing the electrical parameters of ZnO films deposited using a low-cost chemical spray technique through Ta doping, J. Alloy. Compd. 656 (2016) 332–338, http://dx.doi.org/10.1016/j.jallcom.2015.09.115.

[19] Y. Wu, C. Li, M. Li, H. Li, S. Xu, X. Wu, B. Yang, Microstructural and optical properties of Ta-doped ZnO films prepared by radiofrequency magnetron sputtering, Ceram. Int. 42 (2016) 10847–10853, http://dx.doi.org/10.1016/j.ceramint.2016.03.214.

[20] M. Ghosh, A.K. Raychaudhuri, Structure and optical properties of Cd-substituted ZnO (Zn1–xCdxO) nanostructures synthesized by the high-pressure solution route, Nanotechnology 18 (2007) 115618, http://dx.doi.org/10.1088/0957-4484/18/11/115618.

[21] M.K. Yadav, M. Ghosh, R. Biswas, A.K. Raychaudhuri, A. Mookerjee, S. Datta, Band-gap variation in Mg- and Cd-doped ZnO nanostructures and molecular clusters, Phys. Rev. B 76 (2007) 195450 10.1103/PhysRevB.76.195450.

[22] T. Kemmitt, B. Ingham, R. Linklater, Optimization of sol–gel-formed ZnO:Al processing parameters by observation of dopant ion location using solid-state 27Al NMR spectrometry, J. Phys. Chem. C 115 (2011) 15031–15039, http://dx.doi.org/10.1021/jp204283k.

[23] T.A. Para, H.A. Reshi, S. Pillai, V. Shelke, Grain size disposed structural, optical and polarization tuning in ZnO, Appl. Phys. A 122 (2016) 730, http://dx.doi.org/10.1007/s00339-016-0256-8.

[24] E.L. Muñoz, D. Richard, P.D. Eversheim, M. Rentería, Experimental and ab initio study of Ta-doped ZnO semiconductor, Hyperfine Interact. 197 (2010) 181–186, http://dx.doi.org/10.1007/s10751-010-0261-9.

[25] A.S. Mohammadi, S.M. Baizaee, H. Salehi, Density functional approach to study electronic structure of ZnO single crystal, World Appl. Sci. J. 14 (2011) 1530–1536 (ISSN 1818-4952).

[26] Y. Abreu, C.M. Cruz, P. Van Espen, C. Pérez, I. Piñera, A. Leyva, A.E. Cabal, Electric field gradient calculations in ZnO samples implanted with ^{111}In(111Cd), Solid State Commun. 152 (2012) 399–402, http://dx.doi.org/10.1016/j.ssc.2011.12.001.

[27] G.-Y. Huang, C.-Y. Wang, J.-T. Wang, Detailed check of the LDA + U and GGA + U corrected method for defect calculations in wurtzite ZnO, Comput. Phys. Commun. 183 (2012) 1749–1752, http://dx.doi.org/10.1016/j.cpc.2012.03.017.

[28] L.N. Bai, B.J. Zheng, J.S. Lian, Q. Jiang, First-principles calculations of Cd-doped ZnO thin films deposited by pulse laser deposition, Solid State Sci. 14 (2012) 698–704, http://dx.doi.org/10.1016/j.solidstatesciences.2012.03.018.

[29] A. Calzolari, M. Buongiorno Nardelli, Dielectric properties and Raman spectra of ZnO from a first principles finite-differences/finite-fields approach, Sci. Rep. 3 (2013) 2999, http://dx.doi.org/10.1038/srep02999.

[30] J. Xiao, A. Kuc, S. Pokhrel, L. Mädler, R. Pöttgen, F. Winter, T. Frauenheim, T. Heine, Fe-doped ZnO nanoparticles: the oxidation number and local charge on iron, studied by ^{57}Fe Mößbauer spectroscopy and DFT calculations, Chem. Eur. J. 19 (2013) 3287–3291, http://dx.doi.org/10.1002/chem.201204308.

[31] B. Ul Haq, R. Ahmed, S. Goumri-Said, DFT characterization of cadmium doped zinc oxide for photovoltaic and solar cell applications, Sol. Energy Mater. Sol. Cells 130 (2014) 6–14, http://dx.doi.org/10.1016/j.solmat.2014.06.014.

[32] P. Hohenberg, W. Kohn, Inhomogeneous electron gas, Phys. Rev. 136 (1964) B864–B871, http://dx.doi.org/10.1103/PhysRev.136.B864.

[33] W. Kohn, L.J. Sham, Self-consistent equations including exchange and correlation effects, Phys. Rev. 140 (1965) A1133–A1138, http://dx.doi.org/10.1103/PhysRev.140.A1133.

[34] G. Kresse, J. Hafner, Ab initio molecular dynamics for liquid metals, Phys. Rev. B 47 (1993) 558–561, http://dx.doi.org/10.1103/PhysRevB.47.558.

[35] G. Kresse, J. Hafner, Ab initio molecular-dynamics simulation of the liquid-metal amorphous-semiconductor transition in germanium, Phys. Rev. B 49 (1994) 14251–14269, http://dx.doi.org/10.1103/PhysRevB.49.14251.

[36] G. Kresse, J. Furthmüller, Efficiency of ab-initio total energy calculations for metals

and semiconductors using a plane-wave basis set, Compyt. Mater. Sci. 6 (1996) 15–50, http://dx.doi.org/10.1016/0927-0256(96)00008-0.
[37] G. Kresse, J. Furthmüller, Efficient iterative schemes for ab initio total-energy calculations using a plane-wave basis set, Phys. Rev. B 54 (1996) 11169–11186, http://dx.doi.org/10.1103/PhysRevB.54.11169.
[38] J.P. Perdew, K. Burke, M. Ernzerhof, Generalized gradient approximation made simple, Phys. Rev. Lett. 77 (1996) 3865–3868, http://dx.doi.org/10.1103/PhysRevLett.77.3865.
[39] J.P. Perdew, K. Burke, M. Ernzerhof, Generalized gradient approximation made simple, Phys. Rev. Lett. 78 (1997), http://dx.doi.org/10.1103/PhysRevLett.78.1396 (1396-1396).
[40] A. Togo, I. Tanaka, First principles phonon calculations in materials science, Scr. Mater. 108 (2015) 1–5, http://dx.doi.org/10.1016/j.scriptamat.2015.07.021.
[41] D. Porezag, M.R. Pederson, Infrared intensities and Raman-scattering activities within density-functional theory, Phys. Rev. B 54 (1996) 7830–7836, http://dx.doi.org/10.1103/PhysRevB.54.7830.
[42] A. Fonari, S. Stauffer, VASP Raman. 〈https://github.com/raman-sc/VASP/〉, 2013.
[43] M.M.G. Djega-Mariadassou, E. Kerboub, A. Dereigne, M. Gaultier, C.R. Acad. Sci. Paris C 264 (1967) 1753–1755.
[44] A.C. Larson, R.B. Von Dreele, General structure analysis system (GSAS), Los Alamos Natl. Lab. Report. LAUR 86 (2004) 748.
[45] N. Audebrand, J.-P. Auffrédic, D. Louër, X-ray diffraction study of the early stages of the growth of nanoscale zinc oxide crystallites obtained from thermal decomposition of four precursors. General concepts on precursor-dependent microstructural properties, Chem. Mater. 10 (1998) 2450–2461, http://dx.doi.org/10.1021/cm980132f.
[46] E.H. Kisi, M.M. Elcombe, u parameters for the wurtzite structure of ZnS and ZnO using powder neutron diffraction, Acta Crystallogr. C 45 (1989) 1867–1870, http://dx.doi.org/10.1107/S0108270189004269.
[47] A.V. Ghule, B. Lo, S.-H. Tzing, K. Ghule, H. Chang, Y.C. Ling, Simultaneous thermogravimetric analysis and in situ thermo-Raman spectroscopic investigation of thermal decomposition of zinc acetate dihydrate forming zinc oxide nanoparticles, Chem. Phys. Lett. 381 (2003) 262–270, http://dx.doi.org/10.1016/j.cplett.2003.09.125.
[48] M. Schumm, ZnO-Based Semiconductors Studied by Raman spectroscopy: Semimagnetic Alloying, Doping, and Nanostructures (Thesis), Julius Maximilians Universität Wurzburg, Bavaria, 2008.
[49] C. Joseph, P. Bourson, M.D. Fontana, Amorphous to crystalline transformation in Ta_2O_5 studied by Raman spectroscopy, J. Raman Spectrosc. 43 (2012) 1146–1150, http://dx.doi.org/10.1002/jrs.3142.
[50] A. Escobedo Morales, E. Sánchez Mora, U. Pal, Use of diffuse reflectance spectroscopy for optical characterization of un-supported nanostructures, Rev. Mex. Física 53 (2007) 18–22.
[51] Y. Cheng, L. Cao, G. He, G. Yao, X. Song, Z. Sun, Preparation, microstructure and photoelectrical properties of tantalum-doped zinc oxide transparent conducting films, J. Alloy. Compd. 608 (2014) 85–89, http://dx.doi.org/10.1016/j.jallcom.2014.03.031.
[52] J. Lee, J.-H. Hwang, J.J. Mashek, T.O. Mason, A.E. Miller, R.W. Siegel, Impedance spectroscopy of grain boundaries in nanophase ZnO, J. Mater. Res. 10 (1995) 2295–2300, http://dx.doi.org/10.1557/JMR.1995.2295.
[53] A. Ce-Wen Nan, S. Tschöpe, H. Holten, Kliem, R. Birringer, Grain size-dependent electrical properties of nanocrystalline ZnO, J. Appl. Phys. 85 (1999) 7735, http://dx.doi.org/10.1063/1.370578.
[54] N. Al-Hardan, M.J. Abdullah, A. Abdul Aziz, Impedance spectroscopy of undoped and Cr-doped ZnO gas sensors under different oxygen concentrations, Appl. Surf. Sci. 257 (2011) 8993–8997, http://dx.doi.org/10.1016/j.apsusc.2011.05.078.
[55] R.D. Shannon, Revised effective ionic radii and systematics studies in interatomic distances in alides and chalcogenides, Acta Crystallogr. A 32 (1976) 751–767, http://dx.doi.org/10.1107/S0567739476001551.
[56] T. Biswick, W. Jones, A. Pacu1a, E. Serwicka, J. Podobinski, Evidence for the formation of anhydrous zinc acetate and acetic anhydride during the thermal degradation of zinc hydroxy acetate, $Zn_5(OH)_8(CH_3CO_2)_2 - 4H_2O$ to ZnO, Solid State Sci. 11 (2009) 330–335, http://dx.doi.org/10.1016/j.solidstatesciences.2008.06.018.
[57] Z. Ding, W. Wu, S. Liang, H. Zheng, L. Wu, Selective-syntheses, characterizations and photocatalytic activities of nanocrystalline $ZnTa_2O_6$ photocatalysts, Mater. Lett. 65 (2011) 1598–1600, http://dx.doi.org/10.1016/j.matlet.2011.03.028.
[58] M. Bîrdeanu, A.-V. Bîrdeanu, E. Fagadar-Cosma, C. Enache, I. Miron, I. Grozescu, Structural, morphological, optical and thermal properties of the ZnTa2O6 nanomaterials obtained by solid-state method, Dig. J. Nanomater. Biostruct. 8 (2013) 263–272.
[59] Z. Zhou, K. Kato, T. Komaki, M. Yoshino, H. Yukawa, M. Morinaga, K. Morita, Effects of dopants and hydrogen on the electrical conductivity of ZnO, J. Eur. Ceram. Soc. 24 (2004) 139–146, http://dx.doi.org/10.1016/S0955-2219(03)00336-4.